Dorsal Amygdala Neurotrophin-3 Decreases Anxious Temperament in Primates

Supplement 1

Table of Contents:

Supplementary Discussion

RNA-seq analyses to discovery other AT-related transcripts

Although our focus was on *NTRK3*, this approach also served to implicate molecules that have long been hypothesized to underlie anxiety in the risk to develop anxiety and depressive disorders, and discover new potentially AT-related molecules that currently have no known role in anxiety. For example, significant AT-related transcripts included the inhibitory neurotransmitter receptor subunit, *gamma-aminobutyric acid (GABA) A receptor, alpha 5* (*GABRA5*, Figure S3), and the Alzheimer's associated *amyloid precursor protein* (*APP*; Figure S4). For example, post-hoc investigation of *APP* revealed that 8 different features were significant at p<.005 uncorrected, most of which were clustered at the A-Beta coding end of the transcript (1) (Figure S4).

In support of its hypothesized role in anxiety and anxiety-like behavior, we found an inverse relationship between AT and expression levels of *GABAR5*, which encodes the alpha-5 subunit of the GABA-A receptor. Ce *GABAR5* expression levels are known to be increased in highly anxious mice (2) and decrease after fear conditioning (3), a finding that is accompanied by decreased binding of benzodiazepines, a class of drugs often used to treat anxiety. It has previously been shown that genetic variation influencing expression of this gene has been associated with the anxiolytic response to benzodiazepines (4). And, recent work has demonstrated that, in specific populations of Ce neurons, alpha-5 containing GABA-A receptor complexes mediate the extrasynaptic tonic inhibition that underlies fear generalization (5). These findings are consistent

with the hypothesis put forth by Botta et al. (2015) (5) that experience-dependent changes in the expression of *GABAR5* contribute to anxiety by altering the signal-to-noise ratio of phasic fear-relevant inputs to Ce. The data presented here suggest that these specific aspects of *GABAR5* may be conserved in primate species, and related to the early-life risk factors for the development of anxiety and depressive disorders.

This discovery-based approach can also be used to identify AT-related expression levels of transcripts that have not previously been demonstrated to be anxiety-related. For example, we identified amyloid precursor protein (*APP*) as inversely associated with AT. *APP* is most frequently associated with Alzheimer's disease and the accumulation of amyloid deposits that result from cleaving the Aβ portion of the *APP* gene (6). Examination of the portions of the gene that were predictive of AT revealed that it was specifically the Aβ coding portion of the gene that was associated with AT (1). Cleavage products of the Aβ protein can regulate neuronal function and synaptic plasticity (7). Recent evidence suggests that portions of the APP protein bind to a specific sub-component of the metabotropic GABA type B receptor (GABBR1), which was also found to significantly predict AT in our dataset (p=.037; see Table S2). Our APP-$GABA_BR1a$ data suggest the normative function of *APP* within the Ce may play a role in the neural instantiation of dispositional anxiety. These examples highlight the utility of this discovery-based approach, but ultimately mechanistic studies that demonstrate causality will determine their success.

In addition to these transcripts, many others could be of potential interest. To further explore the relationship between relevant AT-related transcripts and AT-related metabolism, we

correlated AT-related exon expression in genes of interest with metabolism throughout the AT circuit. These exploratory analyses revealed brain metabolism distributed throughout the AT-network to be associated with expression of various AT-related genes (see http://at.psychiatry.wisc.edu, or https://github.com/asfox/AT_DorsalAmygdala_RNAseq_FoxEtAl, along with some additional analyses of potential interest and https://www.neurovault.org/collections/AYJGSCJH/).

Supplementary Methods

Method details are broken down by technique as applied in the manuscript.

NEC-FDG: Assessing brain metabolism and AT (and its components) in the NEC context

Individual differences in the anxious temperament (AT) phenotype were quantified using the 30-minute No-Eye-Contact (NEC) condition of the human intruder paradigm (8-10). Subjects were placed in a testing cage, and an experimenter entered the room and stood motionless ~2.5 meters from the subject while presenting his profile and avoiding direct eye contact. Subjects were allowed to freely respond to this ethologically-relevant potential threat, similar to procedures used to assess children's dispositional anxiety and behavioral inhibition in response to a stranger. Anxiety-related behaviors elicited by the NEC challenge were scored by a trained rater, who was blind to monkey group assignment. Freezing was defined as a lack of movement for greater than 3-seconds, and was recorded in seconds / 5-minute epoch of NEC exposure. Mean freezing scores were log-transformed and converted to z-scores. Cooing was measured as the number of coo-vocalizations during each 5-minute epoch of NEC-exposure. Mean cooing frequencies were square-root transformed and converted to z-scores. For the RNA-seq study, but not the NT3-AAV study, freezing and cooing were standardized after covarying for age. This residualization was

not performed for the NT3-AAV study, because we were concerned it would induce more noise as a result of parameter instability, instead we selected animals that were the same age. Plasma cortisol (µg/dL) was quantified based on samples taken immediately after NEC-exposure. Plasma samples collected from animals used in the RNA-seq analysis were assayed for cortisol in duplicate using the DPC Coat-a-count radioimmunoassay (Siemens, Los Angeles, CA). The intra-assay CV% was 4.0 and the inter-assay CV% was 7.0. The limit of detection defined by the lowest standard was 1 µg/dL. The Siemens kit was subsequently discontinued; therefore, plasma samples collected from animals used in the NTF3 viral vector studies were assayed for cortisol in duplicate using the MP Biomedicals (Solon, OH) Immuchem coated tube radioimmunoassay. The intra-assay CV% was 4.9 and the inter-assay CV% was 10.3. The detection limit defined by the lowest standard was 1 µg/dL. In the RNA-seq data, cortisol values were standardized after removing any effects of age, and the time-of-day in which samples were taken. Similar to the behaviors described above, in the NT3-AAV study, cortisol values were not residualized. A composite measure of AT was computed as the average of standardized freezing, cooing and cortisol measures (($Z_{freezing}$ - Z_{cooing} + $Z_{cortisol}$) / 3). This was done across assessments for measures with multiple time-points. Further details on the validation and methods used to assess AT has been previously described (8, 11-13).

In order to measure threat-related metabolic activity animals were restrained in a squeeze cage, intravenously injected with FDG (~7.0 mCi), and then placed in a test cage for 30 minutes, during which time the animals were exposed to NEC. After the 30-minute FDG uptake period, animals were anesthetized with 15 mg/kg of ketamine and 0.04 mg/kg atropine and fitted with an endotracheal tube to maintain isofluorane (1-2%) anesthesia throughout the scanning procedure. Vital signs, including heart rate, oxygen saturation, end tidal CO_2, respiration rate and body temperature, were monitored throughout the scan. RNA sequencing cohorts 1 and 2 were

scanned on a Concorde Microsystems P4 small animal microPET scanner (Siemens, Knoxville, TN) and the NT3 Viral Vector sample was scanned on the Siemens Focus220 microPET scanner. Sixty-minute emission PET scans were reconstructed using standard filtered back projection methods with attenuation- and scatter-correction, and reflect the integrated brain metabolism that occurred during the 30 minutes of FDG uptake. Each native-space FDG-PET image was linearly aligned to its corresponding T1 using a rigid-body transformation in ANTS (14, 15) and then aligned to the 592-monkey template using the T1 ® template transformation. The normalized FDG-PET images were scaled to the whole-brain signal using FSL. The grand-mean scaled post-surgical PET images were subtracted from pre-surgical scaled PET images and then all scaled pre, post, post-pre PET images were spatially smoothed with a 4-mm FWHM Gaussian kernel.

MRI acquisition

Prior to MRI acquisition, the monkeys were anesthetized with ketamine (15 mg/kg, IM). The animals were placed in a MRI-compatible stereotaxic frame, administered dexmedetomidine (0.015 mg/kg, IM), and scanned for approximately one hour. Heart rate and oxygen saturation were monitored throughout the scan. Additional doses of ketamine were given as needed throughout the scan to maintain anesthesia. At the end of the scan the dexmedetomidine was reversed with atipamezole (0.15 mg/kg, IM) and animals were removed from the scanner and monitored until they fully recovered from anesthesia.

T1-weighted MRI scans, which were used for across subject registration, were adjusted for the three different cohorts, as seen below.

RNA sequencing cohort 1: Magnetic resonance imaging (MRI) was performed in a 3-Tesla GE Signa EXCITE (GE Healthcare; Waukesha, WI) scanner with a 16-cm quadrature extremity surface coil at the Waisman Laboratory for Brain Imaging and Behavior, in Madison, WI. The head was fixed in the sphinx position using a custom stereotaxic frame. Whole-brain anatomical images were acquired using a T1-weighted Enhanced Fast Gradient Echo 3-Dimensional (efgre3D, with inversion time [TI] = 600 ms, repetition time [TR] = 8.65 ms, echo time [TE] = 1.89 ms, flip angle = 10°, number of excitations [NEX] = 2, field of view [FOV] = 140 mm, matrix = 256 × 224, in-plane resolution = 0.27 mm, slice thickness = 1.0 mm, Spacing Between Slices = 0.5 mm, 248 slices).

RNA sequencing cohort 2: MRI was performed in a 3-Tesla GE DISCOVERY MR750 (GE Healthcare; Waukesha, WI) scanner with a 16-cm quadrature extremity surface coil at the Lane Imaging Laboratory at the HealthEmotions Research Institute (HERI), in Madison, WI. The head was fixed in the sphinx position using a custom stereotaxic frame. Whole-brain anatomical images were acquired using a coronal T1-weighted 3D Fast Spoiled Grass Sequence with IR Preparation (IR-FSPGR, with inversion time [TI] = 600 ms, repetition time [TR] = 11.45 ms, echo time [TE] = 5.4 ms, flip angle = 10°, number of excitations [NEX] = 2, field of view [FOV] = 140 mm, matrix = 256 × 224, in-plane resolution = 0.27 mm, slice thickness = 1.0 mm, Spacing Between Slices = 0.5 mm, 248 slices).

NT3 viral vector sample: MRI was performed in a 3-Tesla GE DISCOVERY MR750 (GE Healthcare; Waukesha, WI) scanner with a custom 8-channel array coil (Clinical MR Solutions; Brookfield, WI, USA) at the Lane Imaging Laboratory at the HERI, in Madison, WI. The head was fixed in the sphinx position using a custom stereotaxic frame that fit inside the coil. Whole-brain anatomical images were acquired using a coronal T1-weighted 3D Fast Spoiled Grass Sequence with IR Preparation (IR-FSPGR, with inversion time [TI] = 600 ms, repetition time [TR] = 11.92 ms, echo time [TE] = 5.4 ms, flip angle = 10°, number of excitations [NEX] = 2, field of view [FOV] = 140 mm, matrix = 256 × 224, in-plane resolution = 0.27 mm, slice thickness/gap = 0.5 mm, 248 slices).

Image co-registration

In each study, structural MRI scans were used to ensure accurate co-registration of the FDG-PET images. Structural MRI images were aligned to a rhesus monkey MRI template based on 592 young animals described in Fox et al. (2015) (16) using ANTS (pure cross correlation with a window radius of 2 and a weight of 1, with a Gaussian kernel with sigma 2 applied to the similarity gradient, with a SyN transformation model, and 30x20x20x5 iterations). Rigid body registration was used to align the FDG-PET from each animal to the corresponding structural MRI image with a mutual information algorithm using ANTS. Once the FDG-PET and T1-MRI were in the same space, the nonlinear transformation based on the T1-MRI was applied to produce FDG-PET images in standard space.

Tissue processing and RNA extraction

After the animal was euthanized, the brain was removed and placed in a brain block. Tissue was cut into slabs as previously described (17) and frozen by immediate submersion in dry ice-chilled isopentane. Tissue slabs were stored at -80˚C until use. On the day of dissection, the appropriate slab was slightly thawed on wet ice and then the dorsal amygdala was collected using a circular 3 mm punch tool as previously described (17). RNA was extracted from the tissue punches using RNeasy plus mini kits (Qiagen, Germantown, MD) and processed for RNA-seq library construction.

RNA-seq library construction

RNA-Seq was performed using a modification of the SPIA reaction of the NuGEN Ovation RNAseq V2 kit for cDNA Synthesis, followed by library construction using the NuGEN Rapid no-PCR protocol in a NuGEN Mondrian microfluidics instrument. This method uses linear amplification and amplifies the nucleic acid ~1,000X by the end of library construction. Additionally, the method uses random primers for cDNA synthesis and hence assays non-polyA non-coding RNAs, and can provide near perfect 5'→3' read distribution (18). RNA-Seq libraries were then sequenced to a minimum depth of ~30 million single-end 101 base-pair reads. Replicates of 1ng (~100 cell equivalents) of Universal Human Reference (UHR) RNA (Agilent Technologies Inc., 740000) sequenced using this method had an average pairwise r^2 of 0.92 (18).

Trajectory guide base placement and intraoperative MRI (IMRI)

Placement of the MRI-compatible trajectory guide bases followed previously reported methods (19, 20) modified for targeting dorsal amygdala, and are described in detail in the Supplemental Information accompanying Kalin et al. (2016) (21). The intraoperative targeting was performed using a platform for real-time MR-guided prospective stereotaxy (22) that was initially developed by the University of Wisconsin (23-26). To cover as much of the dorsal amygdala as possible while minimizing treatment to surrounding regions, two 6µl infusions were performed per hemisphere (one anterior target, one posterior target), for a total of 12µl per hemisphere. After each infusion the catheter was removed, and after all infusions were complete the animal was transported back to the surgical suite and the craniotomies were closed.

Before the procedure, the animals were anesthetized with ketamine (up to 20 mg/kg, intramuscular (IM)), prepared for surgery, and then placed in a MRI compatible-stereotaxic frame. The animals were intubated and received isoflurane anesthesia (1–3%, intratracheal (IT)). Atropine sulfate (0.01-0.3 mg/kg, IM) was administered to depress salivary secretion, and buprenorphine (0.01-0.03 mg/kg, IM, repeated every 6-12 hours) was given for analgesia. To maintain fluids and electrolytes, Plasmalyte (up to 10 mg/kg/hr, intravenous (IV)) was administered. Cefazolin (20-25 mg/kg, IM or IV) was administered as a prophylactic antibiotic one day prior to the surgery. Cefazolin was also administered immediately prior to surgery, and then every 6 hours while under anesthesia. All drugs and treatments were given in consultation with veterinary staff. Vital signs (heart rate, respiration, oxygen saturation, and end tidal CO_2) were

continuously monitored. Body temperature was monitored during the surgical procedure and maintained by wrapping the animals for warmth.

Prior to surgery the 3D T1W MRIs were used to visualize target in three planes (sagittal, axial, and coronal) and identify the entry point for the catheter. Intraoperative MRI guidance of the catheter was performed using a pivot point-based MRI compatible external trajectory guide (Navigus^{TM} brain port, Medtronic Inc., Minneapolis, MN). Modifications were made to this system to adapt it for the placement of catheters by the addition of a guiding insert, a customized base to fit the nonhuman primate skull and the addition of a laser alignment pointer that fastens to a micromanipulator. Placement of the MRI-compatible trajectory guide bases was performed in a surgical suite under sterile conditions. Using stereotactic guidance, 11-12 mm in diameter craniotomies were made bilaterally at the planned entry points. Each trajectory guide base was mounted on the skull over the craniotomy with three titanium AutoDrive self-tapping screws (OsteoMed, Addison, TX) and dental acrylic. Surgical gelfoam that was moistened with sterile saline was placed over the craniotomies and the bases were capped with sterile plastic base plugs (Navigus).

Catheter trajectory planning and insertion

The animals were transported from the surgical suite to the MRI suite under anesthesia. Sterile conditions were maintained in the MRI suite during viral vector delivery. A 3-inch circular surface coil (MR Instruments, Minneapolis, MN) was positioned above the animal's head, transverse to the main magnetic field, with the Navigus brain port located near the center of the coil. A sterile

MR-visible alignment guide was inserted into the trajectory guide base. The base constrains the guide such that its proximal tip passes the center of the pivot joint, and the distal end up the guide extends away from the skull. A high-resolution, volumetric roadmap scan was acquired for target identification using a 3D IR GRE MRI scan. After identifying the desired target point in the brain and the location of the pivot point in the high-resolution 3D T1-weighted "roadmap" volume, the prospective stereotaxy tool calculates an "aiming point" outside the skull that is co-linear with the target and alignment guide pivot points and then performs real-time imaging of a plane perpendicular to and centered on the aiming point, allowing the operator to reach into the bore of the magnet and move the alignment guide until its image overlaps with the software-displayed aiming point. This system is built on top of the RTHawk scanner interface (HeartVista, Palo Alto, CA), which permits the implementation of image-guided interventional procedures (27), and the VURTIGO toolkit (Visual Understanding of Real-Time Image Guided Operations, Sunnybrook Health Sciences Centre; Toronto, Canada), an open-source visualization platform that allows simultaneous display and interaction with multiple 3D and 2D datasets (28).

Once the alignment guide was determined to be in position, the base was locked into place, the fluid-filled alignment guide was removed, the remote introducer (Navigus) was fastened to the stem, and a catheter guiding insert was placed in the alignment stem. The catheter for the infusion was threaded through the remote introducer and the guiding insert, and was fastened to the remote introducer by a plastic locking mechanism. FEP Teflon infusion lines (IDEX Health & Science, Oak Harbor, WA) were used to connect the catheter via a pressure sensor transducer to a 100 microliter (µl) Hamilton syringe (Hamilton Company USA, Reno, NV) that was placed in

a MRI-compatible syringe pump attached to the control mechanism of a standard Harvard apparatus PHD 2000 (Holliston, MA). Monitoring of the pressure in the infusion line was performed using the infusion pump controller system (Engineering Resources Group, Inc., Pembroke Pines, FL). A computer was connected to the pump controller for infusion protocol programming, which was connected to a pressure sensor transducer to monitor infusion line pressure at the pump output port. The infusion line was primed with a loading line solution (Dulbecco's phosphate-buffered saline (D-PBS) without Ca^{2+} and Mg^{2+} with 5% glycerol) and the catheter was loaded with the viral vector containing the NT3 construct and the MR visible marker Gadobenate dimeglumine (Gd, MultiHance, Bracco Diagnostics).

The catheter (100mm Valve Tip Catheter, Engineering Resources Group, Inc., Pembroke Pines, FL) was a fused silica cannula with a polyimide tubing tip and was sealed with a retractable glass fiber stylet. Its dimensions were: tip—outer diameter (OD) = 0.40 mm, inner diameter (ID) = 0.345 mm, length = 3.0 mm; shaft—OD = 0.67 mm, ID = 0.45 mm, length = 97.0 mm from ferrule, stylet OD = 0.275 mm.

After pressure in the line was stabilized, the catheter was introduced into the brain, advancing the remote introducer at approximately 10-15 mm/minute. The catheter was advanced two-thirds of the measured depth towards the target for partial insertion, and another targeting 3D T1W MRI was performed to confirm the correct trajectory, and calculate the remaining distance from catheter tip to target. Once confirmed, the catheter was advanced to its final position and

the stylet was retracted. When the pressure reading on the infusion pump controller system stabilized, the infusion began.

The infusate consisted of AAV5-NT3 vector in a solution of D-PBS without Ca^{2+} and Mg^{2+} with 5 % glycerol. To facilitate *in vivo* MRI visualization of the infusion, Gd was mixed with the viral vector to reach final concentration 0.66 mM. A total volume of 6 µl was infused at a steady rate of 1 µl/min per infusion site, for a total of 12 µl per hemisphere. After each infusion the previously described 3D roadmap scan was reacquired for a qualitative visualization of the volumetric infusate delivery region. This sequence provides sensitivity to the contrast-enhanced infusate and sufficient gray/white contrast for easy identification of the infusion's anatomical location. These post infusion scans were used to create the infusion overlap image in Figure 3e in the main manuscript. After all infusions were complete the animal was transported back to the surgical suite. To reduce intracranial pressure and prevent brain swelling, Mannitol (up to 2.0 g/kg, IV) was given as needed. The brain ports were removed and the incision was closed in layers before the animal was allowed to recover from anesthesia. Animals were given buprenorphine twice on the day following the surgery (0.01-0.03 mg/kg, IM). Cefazolin (20-25 mg/kg, IM or IV) or Cephalexin (20-25 mg/kg, oral (PO)) was given twice daily for five days after surgery to prevent infection. The animals were allowed to recover and testing did not commence before 2 months after surgery.

AAV construction

The DNA sequence corresponding to the entire open reading frame of the rhesus NTF3 (GenBank accession #XM_001118191, bases 8 to 1033) was inserted into the viral vector pAAV-MCS (Vector Biolabs, Malvern, PA). Expression of the NTF3 was under control of the CMV promoter, and successful plasmid-driven expression of NTF3 was first confirmed *in vitro* by transfecting HEK293 cells grown on glass coverslips. Forty-eight hours after transfection, the cells were fixed at 4˚C with 4% paraformaldehyde for four days, followed by two 2 min washes with phosphate-buffered saline (PBS). The expression of NTF3 in the HEK293 cells was shown by fluorescent immunocytochemistry. First, cells were permeabilized with a 5 min incubation with 0.25% Triton X-100 (Sigma-Aldrich, St Louis, MO) in PBS followed by two 2 min washes with PBS and then non-specific binding was blocked for one hour with 5% normal donkey serum (Jackson ImmunoResearch, West Grove, PA) in PBS. All subsequent incubation steps were performed in PBS containing 5% normal donkey serum. NTF3 expression was detected using an overnight incubation at 4˚C with a 1:80 dilution of an antigen affinity-purified anti-human NTF3 polyclonal antibody raised in goat (R&D Systems, Minneapolis, MN). Following four 10 min washes with PBS containing 5% normal donkey serum, the cells were incubated at room temperature for two hours with a 1:200 dilution of Alexa Fluor 488 conjugated donkey anti-goat secondary antibody (ThermoFisher Scientific, Waltham, MA). After four 10 min washes with PBS, coverslips were mounted on Superfrost Plus slides with ProLong Gold (ThermoFisher Scientific). Fluorescence was visualized using a DMI6000B microscope (Leica Microsystems, Buffalo Grove, IL). Following confirmation of NTF3 protein expression, the plasmid was then packaged into rAAV5 (Vector Biolabs) with a titer of 1.2×10^{13} genome copies/ml.

NTF3 immunohistochemistry

Animals were euthanized by transcardial perfusion with heparinized PBS at room temperature followed by fixation with 4% paraformaldehyde (PFA) at 4˚C. Brains were removed and PFA fixation was continued overnight at 4˚C. The brains were placed in a brain block and cut into slabs that were subsequently processed through increasing concentrations of sucrose – 10%, 20% and 30%. The approximately 14 mm thick tissue slab containing the amygdala was frozen and cut at 40 microns on a cryostat (CryoStar NX50, ThermoFisher Scientific). Tissue sections were stored in cryoprotectant (40 mM potassium phosphate/11mM sodium phosphate buffer, pH 7.2, containing 30% ethylene glycol and 30% sucrose) at -20˚C until use. To identify neurons that expressed NTF3, immunofluorescence was performed. Cryoprotectant was removed by washing sections for 5 hours with PBS; then non-specific binding was blocked for one hour with 5% normal donkey serum (Jackson ImmunoResearch). This, and all subsequent incubation steps were carried out at room temperature in PBS containing 0.3% Triton X-100 (Sigma-Aldrich, St Louis, MO). After each incubation step, sections received three 10 min washes with PBS. Neurons were identified using an overnight incubation with a 1:2000 dilution of a mouse monoclonal neuronal nuclei (NeuN) antibody (clone A60; MilliporeSigma, Burlington, MA) followed by a one-hour incubation with a 1:250 dilution of Alexa Fluor 647 conjugated donkey anti-mouse secondary antibody (ThermoFisher Scientific). NTF3 expressing cells were then identified using an overnight incubation with a 1:200 dilution of the same R&D systems NTF3 antibody used for the *in vitro* studies described in the preceding paragraph followed by a one-hour incubation with a 1:250 dilution of Alexa Fluor 488 conjugated donkey anti-goat secondary antibody (ThermoFisher Scientific). Finally, cellular nuclei were identified using a 5 min incubation with a 1:5000 dilution

of 4',6-diamidino-2-phenylindole (DAPI). Sections were mounted on Superfrost Plus microscope slides using ProLong Gold. Fluorescence was visualized using an oil emersion 40x object with 1.3 na on an A1R-SI+ confocal microscope (Nikon Instruments, Melville, NY).

RNA-seq alignment and quantification

RNA-seq reads were aligned to the Rhesus genome (MaSuRCA v7) using PerM as described in RseqFlow (29). In short, Reads were iteratively aligned with full sensitivity to eight mismatches to coding exons, coding junctions, introns and intergenic regions according to the Rhesus transcriptome (UNMC v7.6.8). Reads which aligned to coding exons and known junctions in each gene model were summed to provide a raw proxy for gene expression. The number of reads per gene in each animal was normalized both by the rank distribution (quantile) as well as by total number of gene-aligned reads (rpkm).

To provide a more in-depth exploration of isoform expression we described the expression per "feature" where features refer to each unique exon or exon-exon junction in a gene model. While specific isoform level expression requires complete knowledge of the set of exons specific to each isoform in a gene model, analysis of features allows each feature to be independently investigated for its association with anxious temperament.

RNA-seq across subject analyses

Analyses were performed to assess the relationship between gene expression and AT in python using statsmodels (https://github.com/statsmodels/statsmodels/). Because annotation of the

rhesus genome is ongoing, and our understanding of splice variation still developing, we performed gene-level multiple regression analyses to predict AT. Each multiple regression analysis was performed in two steps, 1) nuisance variable age was entered into the model to predict AT, 2) estimated expression levels for each exon were simultaneously entered. The test of interest was the significance of the F-change between step 1 and step 2, which accounts for the variance explained by the exonic expression levels. The degrees of freedom for this model vary depending on the number of exons expressed for each gene. Analyses were restricted to genes where we mapped an average of at least 10 reads across subjects, and at least one read in each animal.

In addition to this primary analysis, we performed a series of non-independent follow-up analyses. These analyses included performing independent regressions to predict AT for each gene, and each annotated feature of the rhesus genome, while controlling for age. These analyses are for exploratory purposes only, as we did not correct for multiple comparisons or account for non-independence. All analyses performed can be examined via our web-resource. Follow-up analyses were performed in relation to NTRK3 expression levels, specifically, using non-parametric spearman's correlations between each gene feature and AT. Ontology analyses were performed in reference to the human genome using the Enrichr tool (30, 31).

Voxelwise FDG-PET across subject analyses

Across subject FDG-PET analyses were performed using fmristat in MATLAB, similar to published reports (see: (8, 11, 16)). Voxelwise regressions were performed to examine the relationship

between FDG-PET metabolism in the NEC context and AT, while controlling for age. Results were thresholded at p<.005, two-tailed uncorrected. To examine the extent to which FDG-AT relationships were representative of our previously published large-scale analysis of the neural correlates of AT, we examined the spatial correlation between the FDG-AT voxelwise map in these animals and the previously reported FDG-AT voxelwise map in a sample of 592 young rhesus monkeys (16).

To identify regions where FDG-PET was associated with dorsal amygdala gene expression, we performed voxelwise correlations between FDG and dorsal amygdala gene expression levels in 46 animals. Because this analysis can provide an unreasonable set of data, we restricted our analysis to a few features of interest (RPS6KA4, NTRK3, GABAR5, PENK, APP, ADRA2C, and HRH1). To get a less computationally intensive overview of the relationship between AT-related metabolism and dorsal amygdala gene expression in other transcripts, we used a region of interest approach. More specifically, we extracted mean metabolism within the AT-related cluster (Table S1), and used the feature-based multiple regression approach described above to predict mean metabolism in each significant region. Results are available on our web-resource (http://at.psychiatry.wisc.edu; https://github.com/asfox/AT_DorsalAmygdala_RNAseq_FoxEtAl).

AAV-NT3 statistical analyses

Changes between pre- and post-surgical measures of AT were computed for the dorsal amygdala AAV5-NTF3 animals and compared to similarly-spaced assessments of the control animals.

Corresponding comparisons were also performed to assess the effects of dorsal amygdala AAV5-NTF3 on the components of AT, i.e. freezing, cooing, and cortisol levels. The effects of NTF3 overexpression were assessed using the statsmodels package in python (https://github.com/statsmodels/statsmodels/).

To assess the effects of dorsal amygdala AAV5-NTF3 on brain metabolism in the infused region, we identified voxels that received infusate (as measured by intra-operative Gd), and examined the relationship between the number of subjects that received infusate in that voxel and the group-difference in metabolic change compared to controls. This analysis identified regions infusion-overlap related group-differences in NEC-context metabolism, such that the infusion-induced metabolic changes were larger in those voxels in which more subjects received infusate (Figure 3e). The effects of NTF3 overexpression on metabolism in the infused region were assessed using the statsmodels package in python (https://github.com/statsmodels/statsmodels/).

Voxelwise analyses to examine the broader effects of NTF3 overexpression on brain metabolism were performed using the fmristat packages in MATLAB, as above (also see: (21)). We first computed the changes in metabolism pre- and post-surgery, and similarly timed assessments in control animals. We then performed group t-tests to compare changes in metabolism between groups. Because these analyses were exploratory, results were thresholded at a liberal $p<.05$ two tailed, uncorrected.

Code availability

All code used for RNA-seq alignment is available by contacting T Souaiaia (tade.souaiaia@gmail.com). All code used for neuroimaging and across subject statistics is available by contacting AS Fox (dfox@ucdavis.edu).

Data availability

All data is publicly available. Raw RNA-seq reads from the dorsal amygdala region of nonhuman primates can be found on NCBI (uploaded upon acceptance). All RNA-seq analyses are available online via our web-resource (http://at.psychiatry.wisc.edu; or from github: https://github.com/asfox/AT_DorsalAmygdala_RNAseq_FoxEtAl). Voxelwise PET analyses can be found on Neurovault (https://www.neurovault.org/collections/AYJGSCJH/). Raw data available upon request from NH Kalin (nkalin@wisc.edu).

Supplementary Figures

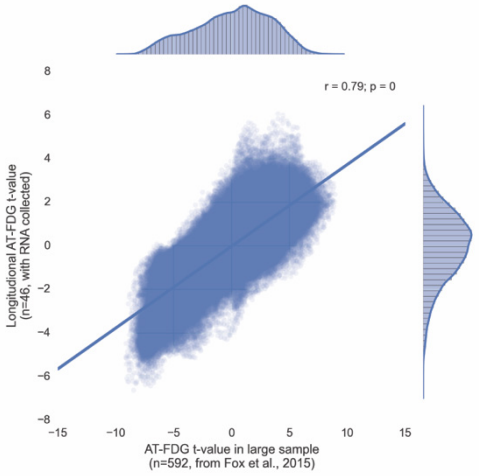

Figure S1: *The spatial distribution of the AT-FDG relationship in these 46 animals was spatially correlated with the distribution of AT-FDG in our previously published large sample of 592 rhesus monkeys.* To identify the regions of the brain where metabolism was associated with AT we performed voxelwise correlations between AT and FDG-PET measures of metabolism during NEC. The histograms and scatter plot for the spatial correlation between these two AT-FDG is seen above.

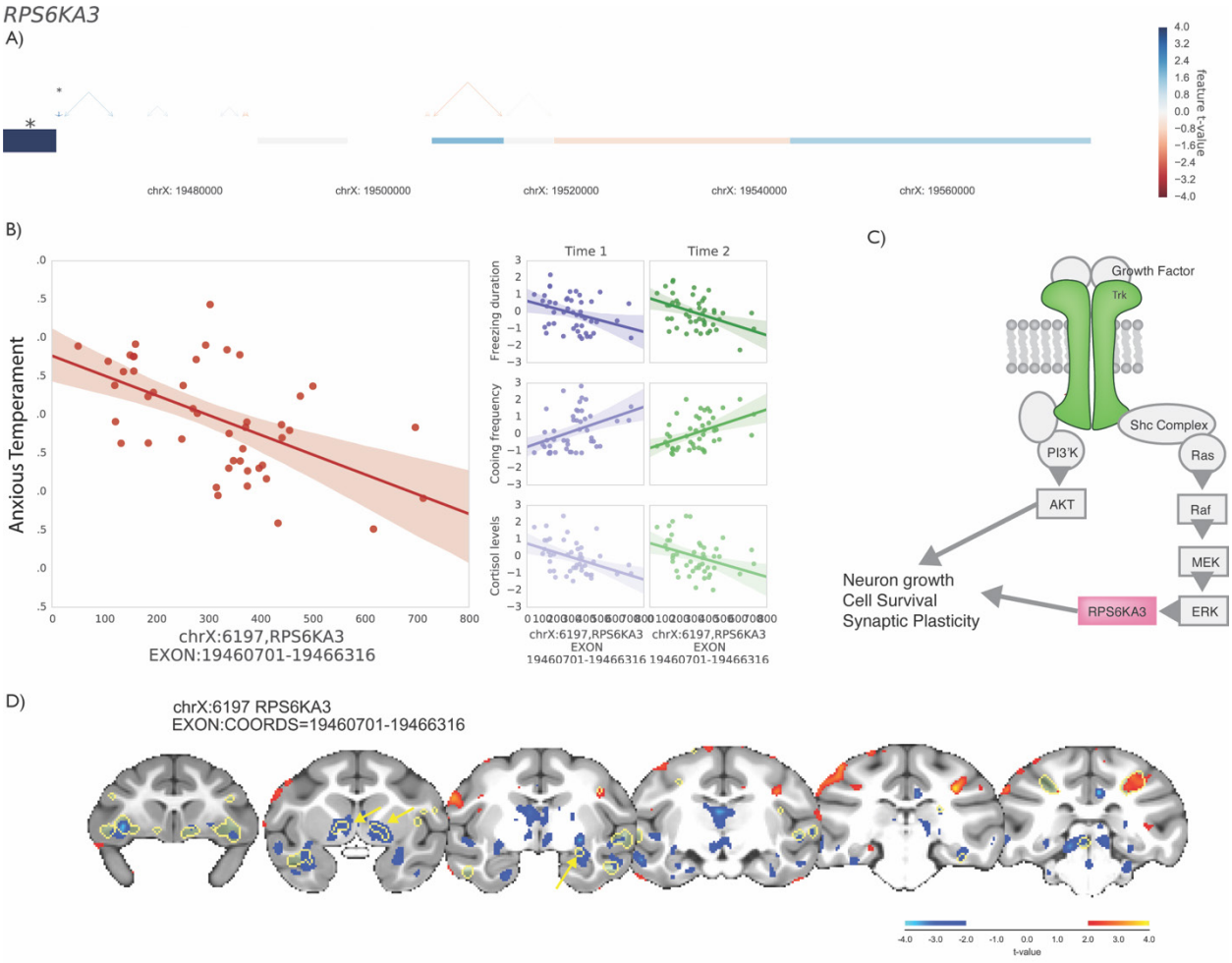

Figure S2: Expression of RPS6KA3, a downstream effector of growth factor receptors, was associated with AT, and its components (n=46). The working gene model for RPS6KA3 (a) with significant regions colored by the t-value of their relationship with AT (a, color-bar). The scatter plots between the most significant exon and anxious temperament (b, left, red scatterplot) as well as for the components of AT (right scatterplots), freezing (top), cooing (middle) and cortisol (bottom) for both time 1 (blue) and time 2 (green). RPS6KA3 is proposed to play a role in tyrosine receptor kinase growth signaling via the MEK-ERK pathway (c). Expression of the most significant RPS6KA3 exon is associated with FDG-PET metabolism (d) throughout the AT-network, as defined by AT-related metabolism from Figure 1 (d; yellow outline), including the dorsal amygdala and bed nucleus of the stria terminalis (yellow arrows). A full un-thresholded voxelwise map can be found on Neurovault.org at: https://www.neurovault.org/collections/AYJGSCJH.

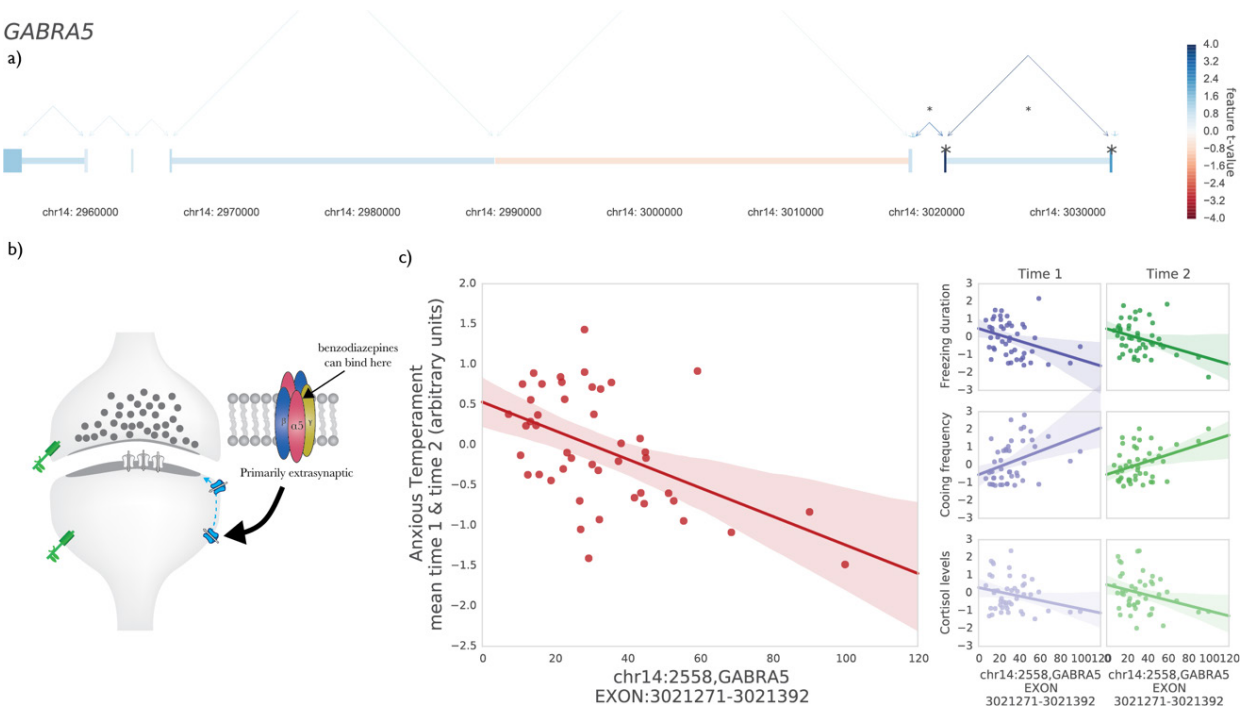

Figure S3: Expression of GABRA5, a GABA-receptor component, was inversely associated with AT, and its components (n=46). The working gene model for GABRA5 (a) with significant regions colored by the t-value of their relationship with AT (a, color-bar). The GABAR5 subunit is primarily expressed on extrasynaptic GABA-receptors in the dorsal amygdala (b, schematic). The scatter plots between the most significant exon and anxious temperament (c, left, red scatterplot) as well as for the components of AT (right scatterplots), freezing (top), cooing (middle) and cortisol (bottom) for both time 1 (blue) and time 2 (green).

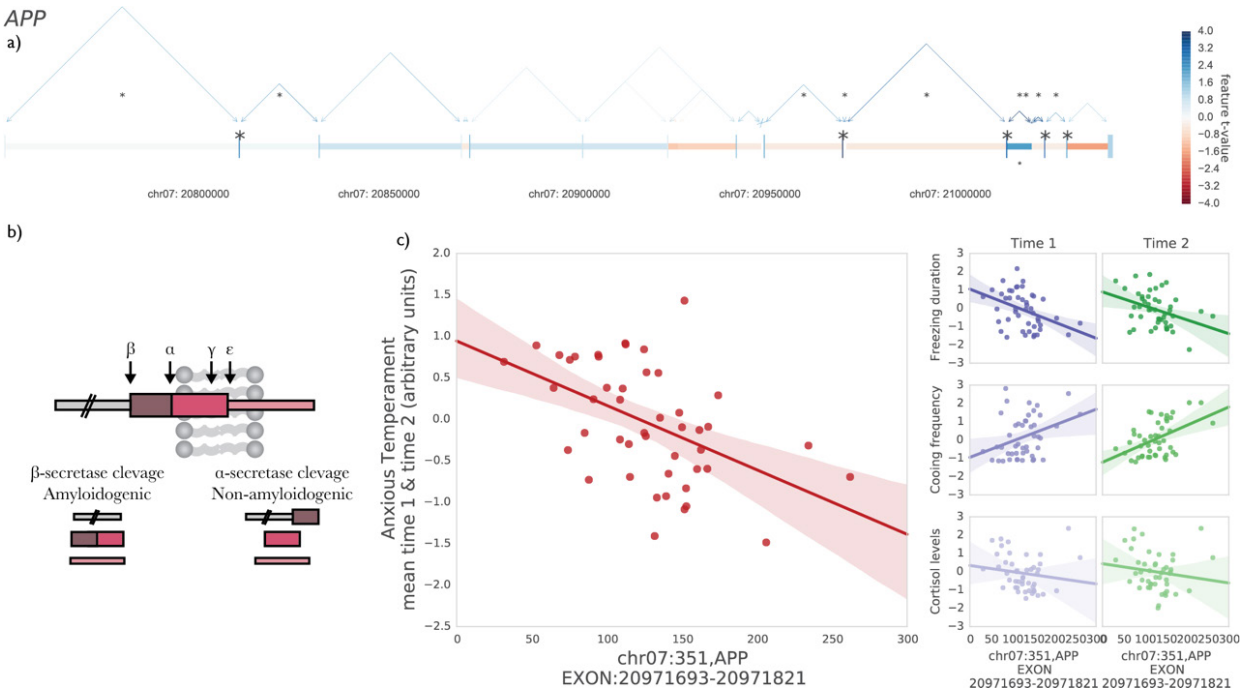

Figure S4: Expression of APP, a gene typically associated with Alzheimer's, was inversely associated with AT, and its components (n=46). The working gene model for APP (a) with significant regions colored by the t-value of their relationship with AT (a, color-bar). The AT-related APP gene features were primarily located near the a/b-secretase cleavage sites (b, schematic). The scatter plots between the most significant exon and anxious temperament (c, left, red scatterplot), as well as for the components of AT (right scatterplots), freezing (top), cooing (middle) and cortisol (bottom) for both time 1 (blue) and time 2 (green).

Supplemental References

1. Dawkins E, Small DH (2014): Insights into the physiological function of the beta-amyloid precursor protein: beyond Alzheimer's disease. *J Neurochem*. 129:756-769.

2. Tasan RO, Bukovac A, Peterschmitt YN, Sartori SB, Landgraf R, Singewald N, et al. (2011): Altered GABA transmission in a mouse model of increased trait anxiety. *Neuroscience*. 183:71-80.

3. Heldt SA, Ressler KJ (2007): Training-induced changes in the expression of GABAA-associated genes in the amygdala after the acquisition and extinction of Pavlovian fear. *Eur J Neurosci*. 26:3631-3644.

4. Clement Y, Prut L, Saurini F, Mineur YS, Le Guisquet AM, Vedrine S, et al. (2012): Gabra5-gene haplotype block associated with behavioral properties of the full agonist benzodiazepine chlordiazepoxide. *Behav Brain Res*. 233:474-482.

5. Botta P, Demmou L, Kasugai Y, Markovic M, Xu C, Fadok JP, et al. (2015): Regulating anxiety with extrasynaptic inhibition. *Nat Neurosci*. 18:1493-1500.

6. O'Brien RJ, Wong PC (2011): Amyloid precursor protein processing and Alzheimer's disease. *Annu Rev Neurosci*. 34:185-204.

7. Kamenetz F, Tomita T, Hsieh H, Seabrook G, Borchelt D, Iwatsubo T, et al. (2003): APP processing and synaptic function. *Neuron*. 37:925-937.

8. Fox AS, Shelton SE, Oakes TR, Davidson RJ, Kalin NH (2008): Trait-like brain activity during adolescence predicts anxious temperament in primates. *PLoS ONE*. 3:e2570.

9. Kalin NH (1993): The neurobiology of fear. *Sci Am*. 268:94-101.

10. Kalin NH, Shelton SE (1989): Defensive behaviors in infant rhesus monkeys: environmental cues and neurochemical regulation. *Science*. 243:1718-1721.

11. Oler JA, Fox AS, Shelton SE, Rogers J, Dyer TD, Davidson RJ, et al. (2010): Amygdalar and hippocampal substrates of anxious temperament differ in their heritability. *Nature*. 466:864-868.

12. Shackman AJ, Fox AS, Oler JA, Shelton SE, Davidson RJ, Kalin NH (2013): Neural mechanisms underlying heterogeneity in the presentation of anxious temperament. *Proceedings of the National Academy of Sciences of the United States of America*. 110:6145-6150.

13. Fox AS, Kalin NH (2014): A Translational Neuroscience Approach to Understanding the Development of Social Anxiety Disorder and Its Pathophysiology. *The American journal of psychiatry*.

14. Avants BB, Tustison NJ, Song G, Cook PA, Klein A, Gee JC (2011): A reproducible evaluation of ANTs similarity metric performance in brain image registration. *NeuroImage*. 54:2033-2044.

15. Avants BB, Yushkevich P, Pluta J, Minkoff D, Korczykowski M, Detre J, et al. (2010): The optimal template effect in hippocampus studies of diseased populations. *NeuroImage*. 49:2457-2466.

16. Fox AS, Oler JA, Shackman AJ, Shelton SE, Raveendran M, McKay DR, et al. (2015): Intergenerational neural mediators of early-life anxious temperament. *Proc Natl Acad Sci U S A*. 112:9118-9122.

17. Fox AS, Oler JA, Shelton SE, Nanda SA, Davidson RJ, Roseboom PH, et al. (2012): Central amygdala nucleus (Ce) gene expression linked to increased trait-like Ce metabolism and anxious temperament in young primates. *Proc Natl Acad Sci U S A*. 109:18108-18113.

18. Dueck HR, Ai R, Camarena A, Ding B, Dominguez R, Evgrafov OV, et al. (2016): Assessing characteristics of RNA amplification methods for single cell RNA sequencing. *BMC Genomics*. 17:966.

19. Emborg ME, Hurley SA, Joers V, Tromp do PM, Swanson CR, Ohshima-Hosoyama S, et al. (2014): Titer and product affect the distribution of gene expression after intraputaminal convection-enhanced delivery. *Stereotact Funct Neurosurg*. 92:182-194.

20. Emborg ME, Joers V, Fisher R, Brunner K, Carter V, Ross C, et al. (2010): Intraoperative intracerebral MRI-guided navigation for accurate targeting in nonhuman primates. *Cell transplantation*. 19:1587-1597.

21. Kalin NH, Fox AS, Kovner R, Riedel MK, Fekete EM, Roseboom PH, et al. (2016): Overexpressing Corticotropin-Releasing Hormone in the Primate Amygdala Increases Anxious Temperament and Alters Its Neural Circuit. *Biol Psychiatry*.

22. Truwit CL, Liu H (2001): Prospective stereotaxy: a novel method of trajectory alignment using real-time image guidance. *Journal of magnetic resonance imaging : JMRI*. 13:452-457.

23. Brodsky EK, Block WF, Alexander AL, Emborg ME, Ross CD, Sillay KA (2011): Intraoperative device targeting using real-time MRI. *Biomedical Sciences and Engineering Conference (BSEC), 2011*, pp 1-4.

24. Grabow B, Block W, Alexander AL, Hurley S, CD R, Sillay K, et al. (2012): Extensible real-time MRI platform for intraoperative targeting and monitoring. *ISMRM Nineteenth Annual Scientific Meeting and Exhibition, poster presentation #1585*. Melbourne, Australia.

25. Grabow BP, Oler JA, Riedel M, Fekete EM, Kovner R, brodsky EK, et al. (2014): Alteration of Molecular Neurochemistry: MRI-guided Delivery of Viral Vectors to the Primate Amygdala. *ISMRM Twenty-First Annual Scientific Meeting and Exhibition, oral presentation #672*. Milan, Italy.

26. Brady ML, Raghavan R, Block W, Grabow B, Ross C, Kubota K, et al. (2015): The Relation between Catheter Occlusion and Backflow during Intraparenchymal Cerebral Infusions. *Stereotact Funct Neurosurg*. 93:102-109.

27. Santos JM, Wright GA, Pauly JM (2004): Flexible Real-Time Magnetic Resonance Imaging Framework.1048-1051.

28. Radau PE, Pintilie S, Flor R, Biswas L, Oduneye SO, Ramanan V, et al. (2012): VURTIGO : Visualization Platform for Real-Time , MRI-Guided Cardiac Electroanatomic Mapping.244-253.

29. Wang Y, Mehta G, Mayani R, Lu J, Souaiaia T, Chen Y, et al. (2011): RseqFlow: workflows for RNA-Seq data analysis. *Bioinformatics*. 27:2598-2600.

30. Chen EY, Tan CM, Kou Y, Duan Q, Wang Z, Meirelles GV, et al. (2013): Enrichr: interactive and collaborative HTML5 gene list enrichment analysis tool. *BMC Bioinformatics*. 14:128.

31. Kuleshov MV, Jones MR, Rouillard AD, Fernandez NF, Duan Q, Wang Z, et al. (2016): Enrichr: a comprehensive gene set enrichment analysis web server 2016 update. *Nucleic Acids Res*. 44:W90-97.